Vibration Estimation of Flexible Space Structures using Range Imaging Sensors

Matthew D. Lichter
Department of Mechanical Engineering
Massachusetts Institute of Technology
Cambridge, MA 02139 USA
lichter@alum.mit.edu

Hiroshi Ueno
Guidance, Control, and Dynamics Group
Japan Aerospace Exploration Agency (JAXA)
Tsukuba, Ibaraki, Japan
ueno.hiroshi@jaxa.jp

Steven Dubowsky
Department of Mechanical Engineering
Massachusetts Institute of Technology
Cambridge, MA 02139 USA
dubowsky@mit.edu

Abstract

Future space applications will require robotic systems to assemble, inspect, and maintain large space structures in orbit. For effective planning and control, robots will need to know the deformation and vibration of the structures with which they interact. This paper presents a method for estimating the shape, motion, and dynamic model parameters of a vibrating space structure using range imaging sensors. The method assumes that the mode shapes are approximately known a priori. An unscented Kalman filter exploits a mechanics-based dynamic model to extract the modal frequencies and damping as well as the modal coefficients and their time rate of change. Both asynchronous-capture (raster-scanning) and synchronous-capture sensors are treated. Theoretical development and experimental results using emulated space hardware are presented.

KEY WORDS—structural dynamics, space structures, range images, identification, unscented Kalman filter

1. Introduction

Future space applications will require autonomous robotic systems to assemble, inspect, and maintain large space structures in orbit (Staritz et al. 2001; Ueno et al. 2003; Mangalgiri 2004). Examples include the International Space Station, large synthetic aperture telescopes, and space solar power systems (Mankins 1997; Oda et al. 2003). Large structures in space tend to be highly flexible and lightly damped (Mangalgiri 2004). To safely plan and execute tasks, robotic systems will require knowledge of the structure's deformations and vibrations. Estimation of target dynamics and model parameters will therefore be a fundamental requirement of these missions.

Many researchers have used embedded sensors such as strain gauges and accelerometers to directly measure the motions and deformations of flexible structures (Maghami and Joshi 1993; Zhang and Wu 1993; Stieber et al. 1996). However, the hardware costs and complexity of this approach may be prohibitive for very large space structures that span hundreds or thousands of meters (Scattolini and Cattane 1999). An alternative approach is to use the range imaging sensors that may be available from free-flying robotic teams (see Figure 1). Such sensors might include stereo cameras (Vergauwen et al. 2003) or laser rangefinders.

Using vision sensors in space is difficult, however. Range images can be highly noisy and data may be absent from many areas of the structure due to the harsh lighting conditions found in space. Strong sunlight, high-contrast scenes, and reflective materials (e.g., solar panels and metallic foils found on spacecraft) pose significant challenges to many image processing algorithms (Jenkin and Jasiobedzki 1998), leading to artifacts such as missing or very noisy data. Tracking specific points on the structure can also be very difficult as the lighting

The International Journal of Robotics Research
Vol. 25, No. 10, October 2006, pp. 1001-1012
DOI: 10.1177/0278364906069100

Figures appear in color online: http://ijr.sagepub.com

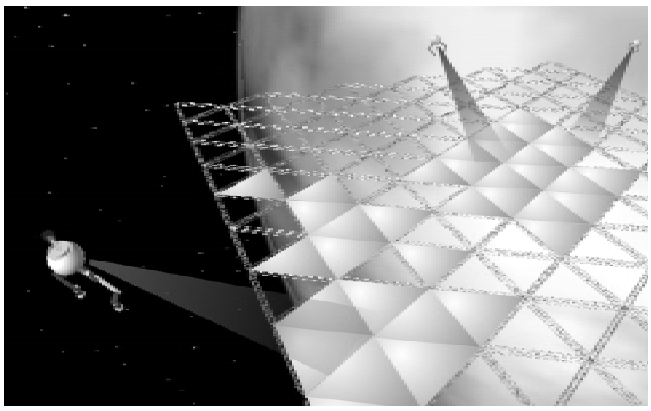

Fig. 1. Using onboard vision sensors to estimate structural information.

or sensor positions change. Further, computational resources tend to be very limited in space-qualified systems.

While some researchers have explored the use of range imaging sensors to estimate the deformations of flexible bodies (Metaxas and Terzopoulis 1993; Tse and Heppler 1992), these methods have either required computational resources beyond those available to space-qualified systems, or have not exploited the highly accurate dynamic model available in this application domain and thus do not provide the motion prediction capabilities necessary for robot planning and control. Moreover, many of the existing methods require the detection of features on the deformable body, which as discussed above may be undesirable for space applications due to robustness concerns.

This paper presents a method for estimating the complete shape and motion of a flexible space structure, using data gathered from one or more 3D range imaging sensors. The method is generalizable to any range imaging sensor as long as its noise statistics (bias and covariance) are well understood (although the characterization of particular sensor implementations is not the focus of this paper). The method described here leverages a key feature of the application, which is that the dynamics of systems in space are highly deterministic and can be modeled accurately. Structural dynamics of space systems are typically analyzed extensively prior to launch through FEM and full-scale experimental testing. This feature allows a method that does not require the tracking of structural features over time. Further, it yields an estimator that is computationally efficient while being robust to substantial sensor noise, missing sensor data, and a priori uncertainty.

2. Estimation Approach

Let the natural mode shapes of the structure be denoted $\Phi_i(x)$ for each mode i. For a linear elastic system, the dynamic response of the structural deformations $z(x,t)$ can be written as

$$z(x,t) = \sum_{i=1}^{m} A_i(t)\,\Phi_i(x) = A(t)^T\,\Phi(x) \tag{1}$$

where $z(x,t)$ is the deflection from the structure's equilibrium state, m is the number of modes excited in the response, and $A_i(t)$ is the ith modal coefficient, which oscillates sinusoidally in time.

The goal is to estimate the time domain functions $A_i(t)$ for all modes of interest. This will reduce shape estimation to simply a modal reconstruction using the estimates of $A_i(t)$ and the known mode shapes $\Phi_i(x)$.

2.1. Assumptions

Sensors are assumed to provide discrete 3D range images of the structure at known intervals. The time at which each point in the image is acquired is assumed to be known. Sensor noise may be substantial and is assumed to be additive and white, but not necessarily Gaussian. This noise may be biased due to sensor localization uncertainty and other factors.

If multiple cooperative sensors are used to gather range images, their relative positions are assumed to be accurately known so that their data can be expressed in a common reference frame. The sensing robots themselves are assumed to carry star sensors, gyroscopes, and other instrumentation to measure the relative kinematics between sensors. It is assumed that the relative position measurements are accurate on the order of one degree in orientation and 1% in distance between sensors, which is readily achievable with many modern technologies. If the sensors are moving with respect to the structure's center of mass, it is assumed this motion is well known.

The structural dynamics of the observed system are assumed to be linear or weakly nonlinear. The modal coefficients $A(t)$ and their time rate of change $V(t)$ are assumed to approximately take the form of decaying sinusoids:

$$\begin{aligned} A_i(t) &\approx e^{-\alpha_i t}\sin(\omega_i t + \varphi_i) \\ V_i(t) \equiv \tfrac{d}{dt}A_i(t) &\approx e^{-\alpha_i t}\omega_i\cos(\omega_i t + \varphi_i) - \alpha_i A_i(t) \end{aligned} \tag{2}$$

where ω_i is the frequency, α_i is the modal damping coefficient, and φ_i is the phase of the ith mode of vibration.

The structure's mode shapes are assumed to be reasonably well-known to the estimator *a priori*. These could be provided from theoretical, numerical, or empirical analysis performed offline. Modal information is assumed to be updated whenever the fundamental mode shapes change (e.g., due to a structural configuration change, added mass, etc.). The modal frequencies are assumed to be known with reasonable certainty *a priori* using conventional analysis tools (i.e., predictions accurate to one significant digit or better).

2.2. Approach

Estimation of $A_i(t)$ occurs here in two steps. First, a modal decomposition in the spatial domain is performed on the range image to arrive at a coarse estimate $\breve{A}_i(t)$. This estimate is then filtered in the time domain using a Kalman filter to arrive at a refined estimate $\hat{A}_i(t)$. Note the hat notation used to denote coarse and refined estimates.

3. Modal Decomposition

The estimation process first uses a modal decomposition of the visual data to compute coarse estimates of the modal coefficients $A(t)$. Define an inner product (generalized dot product) over some space X as

$$\langle a, b\rangle_X \equiv \int_X a(x)\, b(x)\, dx.$$

For notational simplicity in this paper, if the elements in the inner product are vectors of functions, the notation will indicate an expansion as follows:

$$\langle a, b\rangle_X \equiv \int_X a(x)\, b^T(x)\, dx = \int_X \begin{bmatrix} a_1(x)\, b_1(x) & a_1(x)\, b_2(x) & \cdots \\ a_2(x)\, b_1(x) & a_2(x)\, b_2(x) & \\ \vdots & & \ddots \end{bmatrix} dx.$$

Let the space X be the "backbone" surface of the target structure. For example, if the structure is a planar sheet of uniform thickness, then the space X is the 2D reference surface embedded in the sheet at its equilibrium configuration, and $z(x, t)$ represents the deformation normal to the surface at some location x in X and time t. One useful property of mode shapes is that they are orthogonal in the space X (i.e., $\langle \Phi_i, \Phi_j \rangle_X = 0$ for all $i \neq j$).

Consider a subspace $Y \subset X$, which represents a discrete, not necessarily uniform sampling of the space X (see Figure 2). The subspace Y is the sample space defined by the range measurements, and may change over time as the sensor and/or structure move.

In this discrete space the inner product reduces to:

$$\langle a, b\rangle_Y = \sum_{k=1}^{n} a(y_k)\, b^T(y_k)$$

where y_k is the kth discrete point in the sample space Y and n is the total number of discrete points in Y.

Define a symmetric *modal correlation matrix* M_Y to describe the inner products of the mode shapes in the sample space Y, for the m excited modes:

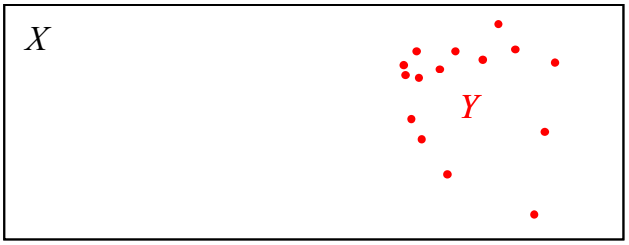

Fig. 2. Sample space Y in complete space X.

$$M_Y \equiv \langle \Phi, \Phi\rangle_Y = \begin{bmatrix} \langle \Phi_1, \Phi_1\rangle_Y & \cdots & \langle \Phi_1, \Phi_i\rangle_Y & \cdots & \langle \Phi_1, \Phi_m\rangle_Y \\ \vdots & \ddots & \vdots & \ddots & \vdots \\ \langle \Phi_i, \Phi_1\rangle_Y & \cdots & \langle \Phi_i, \Phi_i\rangle_Y & \cdots & \langle \Phi_i, \Phi_m\rangle_Y \\ \vdots & \ddots & \vdots & \ddots & \vdots \\ \langle \Phi_m, \Phi_1\rangle_Y & \cdots & \langle \Phi_m, \Phi_i\rangle_Y & \cdots & \langle \Phi_m, \Phi_m\rangle_Y \end{bmatrix}.$$

If Y is dense and uniformly distributed over X, then $M_Y \approx \lambda M_X$ for some scale factor λ. However, this paper treats the general case in which the sample space Y is not a uniform and complete sampling of the complete structure space X (e.g., the sensors observe only a portion of the structure). If the sample space is changing (e.g., the sensors are moving), the modal correlation matrix M_Y and the inner product operator $\langle a, b\rangle_Y$ are not constant and must be recomputed at each time step. Provided the motion is known, such relative sensor movements do not prohibit the application of the proposed method.

By the Cauchy–Schwarz inequality, it can be shown that M_Y is at least positive semidefinite (Lichter 2004). The semidefinite condition arises only from a pathological choice of the sample space Y such that certain modes are unobservable or undiscernable (i.e., the modes are aliased spatially). The condition number of M_Y can be computed to determine the proximity to this condition, and thus the approach yields a convenient method for online assessment of system observability. All further discussion here will assume that M_Y is positive definite, well-conditioned, and invertible.

3.1. Synchronous Sensors

For synchronous sensors that capture all their range data at the same instant in time (e.g., stereo vision systems), sensor measurements can be written as

$$\begin{Bmatrix} \bar{z}(y_1,t) \\ \vdots \\ \bar{z}(y_k,t) \\ \vdots \\ \bar{z}(y_n,t) \end{Bmatrix} = \begin{Bmatrix} z(y_1,t) \\ \vdots \\ z(y_k,t) \\ \vdots \\ z(y_n,t) \end{Bmatrix} + \begin{Bmatrix} c_1 \\ \vdots \\ c_k \\ \vdots \\ c_n \end{Bmatrix} + \begin{Bmatrix} e_1 \\ \vdots \\ e_k \\ \vdots \\ e_n \end{Bmatrix}$$

$$\Leftrightarrow \bar{z} = z + c + e$$

where the overbar is used to denote a measurement, $z(y_k, t)$ is the true deformation of the target at location y_k, c_k is sensor bias due to sensor localization error and other effects, and e_k is white unbiased sensor noise.

The modal coefficients $A(t)$ can be recovered through an inner product of the mode shapes with the true deformation of the target:

$$\langle \Phi, z \rangle_Y \equiv \begin{Bmatrix} \langle \Phi_1, z \rangle_Y \\ \vdots \\ \langle \Phi_i, z \rangle_Y \\ \vdots \\ \langle \Phi_m, z \rangle_Y \end{Bmatrix} = M_Y A(t)$$

$$\Rightarrow A(t) = M_Y^{-1} \langle \Phi, z \rangle_Y .$$

Substituting noisy measurements into this equation yields

$$\breve{A}(t) = M_Y^{-1} \langle \Phi, \bar{z} \rangle_Y = A(t) + b + w \tag{3}$$

where a nonrandom bias vector is defined $b \equiv M_Y^{-1} \langle \Phi, c \rangle_Y$ and a random noise vector is defined $w \equiv M_Y^{-1} \langle \Phi, e \rangle_Y$. By the central limit theorem w is a Gaussian random variable since the number of points in the range image is typically large. Since noise e is white and unbiased, $E[w] = 0$. However, $b \neq 0$ in general, so it can be said that (3) is a biased estimator of $A(t)$, with bias linearly related (by its mathematical definition) to sensor localization error and other sources of sensory bias.

The covariance on the coarse estimate $\breve{A}(t)$ is given by

$$\Lambda_{ww} \equiv E\left[w \cdot w^T\right] = M_Y^{-1} E\left[\langle \Phi, e \rangle_Y \langle e, \Phi \rangle_Y\right] M_Y^{-1} \tag{4a}$$

If the variance on the noise e is approximately the same for all range image points, this simplifies to

$$\Lambda_{ww} = \sigma_e^2 M_Y^{-1} \tag{4b}$$

where $\sigma_e^2 \equiv E\left[e_k^2\right]$. If the noise variance is substantially different for each range image point, the equations are not as concise but Λ_{ww} is still easily solved (Lichter 2004). Such a situation could arise in practice, for example, if the sensors were located at substantially different viewing distances from the structure.

3.2. Asynchronous Sensors

Many conventional sensors do not capture all their data at the same instant in time, but rather perform asynchronous capture of each point in the range image. For example, raster-scanning laser-based systems capture their data sequentially, creating non-negligible delays between the times at which each point in the range image is captured. For linear and weakly nonlinear dynamic structures, the mathematical effects of these delays can be manipulated so that the methods discussed in the previous section remain applicable.

For asynchronous sensors, a vector of range image points is provided to the estimator at some reference time t. The kth element of the vector (the kth point) measures the displacement of the structure at some location y_k and time $t + \Delta_k$, where Δ_k is a known time delay due to the asynchronicity of capture. The k^{th} sensor measurement can be written as

$$\begin{aligned} \bar{z}_k(t) &= \left(\sum_{i=1}^{m} A_i(t + \Delta_k)\, \Phi_i(y_k)\right) + c_k + e_k \\ &= A(t + \Delta_k)^T\, \Phi(y_k) + c_k + e_k \end{aligned} \tag{5}$$

where $A(t + \Delta_k)$ is the vector of modal coefficients at time $t + \Delta_k$, $\Phi(y_k)$ is the vector of mode shapes evaluated at location y_k, and c_k and e_k are additive sensor bias and noise as before. It is assumed that the delays Δ_k are known reasonably well for all k, although there are no special requirements on the uniformity of these delays.

Applying trigonometric substitutions to (2) yields

$$A_i(t + \Delta_k) = A_i(t)\, f_i(\Delta_k) + V_i(t)\, g_i(\Delta_k) \tag{6}$$

where f_i and g_i are delay modulation functions given by

$$\begin{aligned} f_i(\Delta_k) &= e^{-\alpha_i \Delta_k}\left(\cos(\omega_i \Delta_k) + \frac{\alpha_i \sin(\omega_i \Delta_k)}{\omega_i}\right) \\ g_i(\Delta_k) &= e^{-\alpha_i \Delta_k}\left(\frac{\sin(\omega_i \Delta_k)}{\omega_i}\right) \end{aligned} \tag{7}$$

Predicted values are adequate for the frequency and damping terms in (7), so these functions can be considered reasonably well known a priori. Substituting (6) into (5) yields

$$\begin{aligned} \bar{z}_k(t) = &\sum_{i=1}^{m} A_i(t)\, f_i(\Delta_k)\, \Phi_i(y_k) \\ &+ \sum_{i=1}^{m} V_i(t)\, g_i(\Delta_k)\, \Phi_i(y_k) + c_k + e_k \end{aligned} . \tag{8}$$

Define the *delay-modulated mode shapes*

$$\begin{aligned} \Phi_i^f(y_k, \Delta_k) &\equiv f_i(\Delta_k)\, \Phi_i(y_k) \\ \Phi_i^g(y_k, \Delta_k) &\equiv g_i(\Delta_k)\, \Phi_i(y_k) \end{aligned} .$$

These can be viewed as fundamental mode shapes in the space-time domain (as opposed to the original modes $\Phi_i(y_{k'})$, which reside strictly in the spatial domain). Equation (8) can now be written in the compact form

$$\bar{z}_k(t) = \begin{Bmatrix} A(t) \\ V(t) \end{Bmatrix}^T \begin{Bmatrix} \Phi^f(y_k, \Delta_k) \\ \Phi^g(y_k, \Delta_k) \end{Bmatrix} + c_k + e_k \tag{9}$$

which has obvious similarity to (1). In this form, one can readily apply the approach of the previous section to yield an estimator analogous to (3):

$$\begin{Bmatrix} \breve{A}(t) \\ \breve{V}(t) \end{Bmatrix} = M_Y'^{-1} \begin{Bmatrix} \langle \Phi^f, \bar{z} \rangle_Y \\ \langle \Phi^g, \bar{z} \rangle_Y \end{Bmatrix}$$

$$= \begin{Bmatrix} A(t) \\ V(t) \end{Bmatrix} + b' + w' \tag{10}$$

where the bias b' and error w' are given by

$$b' \equiv M_Y'^{-1} \begin{Bmatrix} \langle \Phi^f, c \rangle_Y \\ \langle \Phi^g, c \rangle_Y \end{Bmatrix} \qquad w' \equiv M_Y'^{-1} \begin{Bmatrix} \langle \Phi^f, e \rangle_Y \\ \langle \Phi^g, e \rangle_Y \end{Bmatrix}$$

and the *delay-modulated modal correlation matrix* M_Y' is given by

$$M_Y' \equiv \begin{bmatrix} \langle \Phi^f, \Phi^f \rangle_Y & \langle \Phi^f, \Phi^g \rangle_Y \\ \langle \Phi^g, \Phi^f \rangle_Y & \langle \Phi^g, \Phi^g \rangle_Y \end{bmatrix}.$$

Analogous to (4), the error covariance on the estimate given by (10) is

$$\Lambda_{ww} \equiv E\left[w' \cdot w'^T \right] \tag{11a}$$

$$= M_Y'^{-1} E\left(\begin{bmatrix} \langle \Phi^f, e \rangle_Y \langle e, \Phi^f \rangle_Y & \langle \Phi^f, e \rangle_Y \langle e, \Phi^g \rangle_Y \\ \langle \Phi^g, e \rangle_Y \langle e, \Phi^f \rangle_Y & \langle \Phi^g, e \rangle_Y \langle e, \Phi^g \rangle_Y \end{bmatrix} \right) M_Y'^{-1}.$$

As before, if the variance on the noise e is approximately the same for all image points, this simplifies to

$$\Lambda_{ww} = \sigma_e^2 M_Y'^{-1}. \tag{11b}$$

4. Kalman Filtering: Sinusoid Estimation

Equation (3) or (10) provides an easily computed coarse estimate of $A(t)$ (and $V(t)$ for asynchronous sensors) that has a Gaussian error distribution with statistics computed from (4) or (11). It is a minimum-variance estimate of $A(t)$ (and $V(t)$) using data from a single sample time.

A Kalman filter is used to refine the estimates of $A(t)$ (and $V(t)$) using knowledge that they are weakly decaying sinusoids measured with some bias. Observation over time allows the identification of this bias as well as modal parameters such as frequency and damping.

The estimated state consists of $\hat{A}(t)$, its time rate of change $\hat{V}(t)$, the natural frequencies $\hat{\omega}$, the modal damping rate $\hat{\alpha}$, and the measurement bias $\hat{b}$ (or $\hat{b}'$ if using asynchronous sensors). If the true modal coefficients follow the trajectory given by (2), differentiation and substitution leads to the discrete-time process model

$$\begin{Bmatrix} A_i \\ V_i \\ \omega_i \\ \alpha_i \\ b_i \end{Bmatrix}_{(t+\Delta)} =$$

$$\begin{Bmatrix} \exp(-\Delta\alpha_i) \cdot \left(A_i \cos(\Delta\omega_i) + \frac{(V_i + \alpha_i A_i)}{\omega_i} \sin(\Delta\omega_i) \right) \\ \exp(-\Delta\alpha_i) \cdot \left(V_i \cos(\Delta\omega_i) - \frac{\alpha_i V_i + (\omega_i^2 + \alpha_i^2) A_i}{\omega_i} \sin(\Delta\omega_i) \right) \\ \omega_i \\ \alpha_i \\ b_i \end{Bmatrix}_{(t)}$$

$$+ v_i. \tag{12}$$

Note the lack of dependence on phase φ_i. If known external forces are applied to the structure (e.g., from robotic systems), they should be incorporated into the process model here. Process noise is indicated in (12) by $v \equiv \begin{Bmatrix} v_A & v_V & v_\omega & v_\alpha & v_b \end{Bmatrix}^T$, and is characterized by the covariance matrix

$$\Lambda_{vv} \equiv E\left[v v^T \right]. \tag{13}$$

The values in this matrix should be chosen to reflect expected magnitudes of disturbances, modeling uncertainty, and measurement bias drift due to sensor motion with localization uncertainty.

The Kalman filter measurement model is given by (3) or (10). Measurement noise w is white, unbiased, and Gaussian with statistics computed from (4) or (11).

The initial a posteriori state estimate is given by

$$\begin{Bmatrix} \hat{A}(0) & \hat{V}(0) & \hat{\omega}(0) & \hat{\alpha}(0) & \hat{b}(0) \end{Bmatrix}^T =$$

$$\begin{Bmatrix} \breve{A}(0) & \breve{V}(0) & \hat{\omega}_{exp} & \hat{\alpha}_{exp} & 0 \end{Bmatrix}^T \tag{14}$$

where ω_{exp} and α_{exp} are the expected frequencies and damping from *a priori* predictions. For synchronous sensors, no coarse estimate $\breve{V}(0)$ exists, and the estimate should instead be initialized to the unbiased value of zero.

The initial *a posteriori* state estimate error covariance should be chosen to describe the uncertainty in (14). The covariance on $\hat{A}(0)$ (and $\hat{V}(0)$) will be the measurement covariance given by (4) or (11) while the other elements of the state covariance matrix must be based on engineering judgment of the system.

The implementation of the Kalman filter is straightforward using (3), (4), and (10)–(14). Since the process model is nonlinear, an extended Kalman filter, unscented Kalman filter, particle filter, or a more general form of Bayesian estimator must be used. The unscented Kalman filter (Julier and Uhlmann 1997) is easy to implement, has low computational burden, and was observed to perform well in our studies.

5. Shape Estimation: Modal Reconstruction

Shape estimation is simply a modal reconstruction using (1) and the estimated modal coefficients:

$$\hat{z}(x,t) = \sum_{i=1}^{m} \hat{A}_i(t)\,\hat{\Phi}_i(x) = \hat{A}(t)^T\,\hat{\Phi}(x). \qquad (15)$$

The hat notation is used on the mode shapes $\Phi(x)$ as a reminder that these functions are not known perfectly, as they are based on *a priori* predictions of structural dynamics.

If mode shapes are known to very high accuracy, the uncertainty in the shape estimate due to coefficient estimation errors is given by

$$\Lambda_{zz}(x,t) \equiv E\left[\left(\hat{z}(x,t) - z(x,t)\right)\left(\hat{z}(x,t) - z(x,t)\right)^T\right] = \Phi(x)^T\,\Lambda_{\hat{A}\hat{A}}(t)\,\Phi(x) \qquad (16)$$

where $\Lambda_{\hat{A}\hat{A}}(t)$ is the standard output of the Kalman filter that describes the error covariance on the estimate $\hat{A}(t)$.

In practice however, nonlinearities, parameter uncertainty, and model simplifications lead to errors in the predicted mode shapes. Define the following relation between the predicted and actual mode shapes:

$$\Gamma_k\hat{\Phi}(x) \equiv \Phi(x) + \delta_k(x) \qquad (17)$$

where $\delta_k(x)$ represents a small error displacement function. The scaling matrix Γ_k is approximately the identity and is chosen so the following is satisfied:

$$\left\langle \hat{\Phi}, \delta_k \right\rangle_{Y_k} \equiv [0]. \qquad (18)$$

Figure 3 shows a graphical interpretation of these equations. Note that in order to satisfy (17), $\delta_k(x)$ and Γ_k will change slightly whenever the sample space Y changes.

Ignoring sensory error and looking only at the effects of a priori mode shape error, the expected estimate of the modal coefficients $A(t)$ is given by

$$E\left\{\hat{A}(t)\right\} = \hat{M}_Y^{-1}\left\langle \hat{\Phi}, z \right\rangle_Y$$

where the predicted mode shapes are used in the predicted modal correlation matrix $\hat{M}_Y$. The expected value of the shape estimate is thus

$$E\left\{\hat{z}(x,t)\right\} = E\left\{\hat{A}(t)\right\}^T\hat{\Phi}(x) = \left[\hat{M}_Y^{-1}\left\langle \hat{\Phi}, z \right\rangle_Y\right]^T\hat{\Phi}.$$

Consider the following metric ε_B for quantifying the magnitude of the shape estimation error due to imperfect mode shape knowledge:

$$\varepsilon_B \equiv \frac{\left\|E\left(\hat{z}\right) - z\right\|_B}{\|z\|_B} \qquad (19)$$

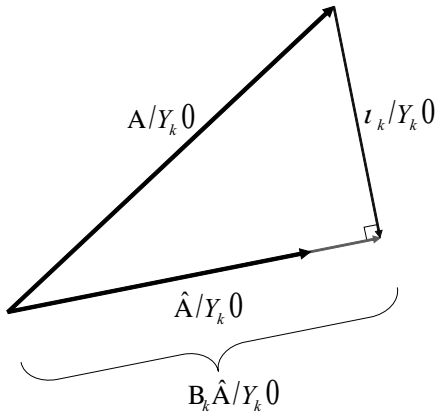

Fig. 3. Graphical interpretation of (17) and (18).

where the double brackets indicate the norm of the enclosed value over the subscripted space. That is,

$$\|a\|_B \equiv \sqrt{\langle a, a\rangle_B}.$$

Equation (19) thus defines a ratio between the RMS shape estimation error and the RMS amplitude of vibration at one instant in time. The space B could be X, Y, or any other space over which one would like to compute shape error. The denominator of (19) can be computed as

$$\|z\|_B = \sqrt{\langle z, z\rangle_B} = \sqrt{A^T\,\langle\Phi, \Phi\rangle_B\,A}. \qquad (20)$$

The numerator of (19) is computed as

$$\begin{aligned}\left\|E\left(\hat{z}\right) - z\right\|_B &= \left\|\left[\hat{M}_Y^{-1}\left\langle\hat{\Phi}, z\right\rangle_Y\right]^T\hat{\Phi} - A^T\Phi\right\| \\ &= \left\|A^T\left(\left\langle\Phi, \hat{\Phi}\right\rangle_Y\hat{M}_Y^{-1}\hat{\Phi} - \Phi\right)\right\| \\ &= \left\|A^T\left(\left\langle\Gamma_k\hat{\Phi} - \delta_k, \hat{\Phi}\right\rangle_Y\hat{M}_Y^{-1}\hat{\Phi} - \left(\Gamma_k\hat{\Phi} - \delta_k\right)\right)\right\| \\ &= \left\|A^T\delta_k\right\|\end{aligned}$$

$$\left\|E\left(\hat{z}\right) - z\right\|_B = \sqrt{A^T\,\langle\delta_k, \delta_k\rangle_B\,A} \qquad (21)$$

Substituting (20) and (21) into (19) yields

$$\varepsilon_B = \sqrt{\frac{A^T\,\langle\delta_k, \delta_k\rangle_B\,A}{A^T\,\langle\Phi, \Phi\rangle_B\,A}}.$$

Examining order of magnitude relationships between estimation error and mode shape uncertainty reveals

$$\begin{aligned}O(\varepsilon_B) &= O\left(\sqrt{\frac{A^T\,\langle\delta_k, \delta_k\rangle_B\,A}{A^T\,\langle\Phi, \Phi\rangle_B\,A}}\right) \\ &\approx O\left(\sqrt{\frac{|\langle\delta_k, \delta_k\rangle_B|_{Fro}}{|\langle\Phi, \Phi\rangle_B|_{Fro}}}\right) \approx O\left(\frac{\|\delta_k\|_B}{\|\Phi\|_B}\right)\end{aligned} \qquad (22)$$

where single brackets with subscript *Fro* indicate the Frobenius (matrix) norm.

This result suggests that estimation errors arising from imperfect modal knowledge are directly proportional to the ratio between mode shape errors and the mode shape amplitudes. This suggests that estimator performance degrades gracefully rather than catastrophically as mode shape uncertainty grows.

6. Results

A number of simulation and experimental studies were used to evaluate the performance and practicality of the proposed estimation methods.

6.1. Simulation Results

Computer simulations were used to study estimator performance under a wide range of sensing conditions. Representative space structures were built into a virtual environment created with OpenGL. Structural models used here are representative of state-of-the-art deployable space structures (Mangalgiri 2004). Figure 4 shows a simulated structure that is representative in scale and stiffness of proposed space solar power systems (Mankins 1997; Oda et al. 2003). Each triangular element has a 200 m side length, yielding a structure approximately 2 km by 2 km in size. The first mode of vibration has a period of approximately 250 minutes and the one-hundredth mode has a period of approximately 250 seconds. The modes were energy-normalized so that a modal coefficient of 1.0 indicated the same elastic energy for each mode. The simulated structure was given a random excitation on the interval $0 \leqslant A_{i_{\max}} \leqslant 1$, yielding uniform expected energy for all modes. Phase for each mode was randomly selected over the interval $0 \leqslant \varphi_i < 2\pi$. For initial studies, damping was zero, all active modes were estimated, and the mode shapes were known perfectly by the estimator.

A single simulated sensor was placed in this environment and its range images were synthesized. The sensor had a resolution of 30 by 30 pixels and a field of view of 80°. The sensor was placed so that it observed approximately one-quarter of the structure (see Figure 4). Range images were taken at a rate of one per simulated minute. Gaussian noise was added to the synthetic range images, with a standard deviation of 3% of the measurement in the range direction. This value is similar to that found in practical sensors proposed for space applications (Vergauwen et al. 2003; Wakabayashi et al. 1999).

Figure 5 shows typical simulation results for the surrogate measurements $\breve{A}(t)$ and filtered estimates $\hat{A}(t)$ of three modal coefficients. These results are similar for all modes, regardless of number estimated, as long as the Nyquist sampling criterion is met with respect to the modal frequencies. Note that the signal-to-noise ratio is different for each mode due to the sample space chosen, which affects the matrix M_Y and therefore the noise on the surrogate measurement (see (4b)).

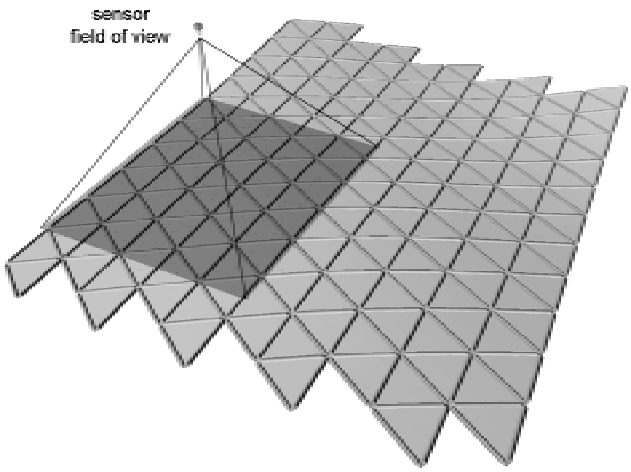

Fig. 4. Planar space structure used in simulation studies. Vibrations occur out-of-plane. Simulated range imager and its field of view are shown.

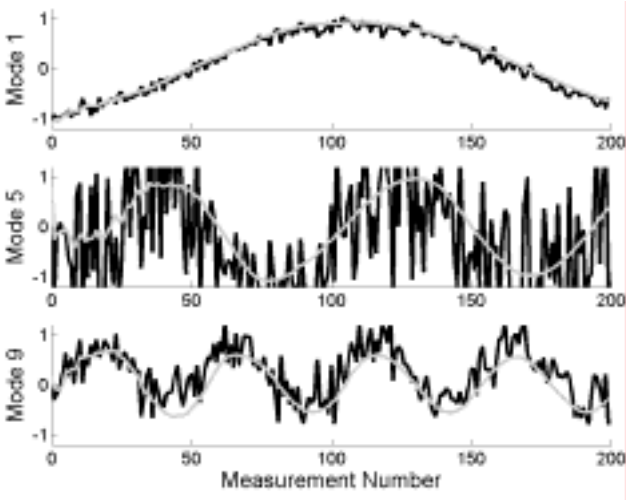

Fig. 5. Surrogate measurements of modal coefficients (black lines), with results of Kalman filtering superimposed (gray lines) (simulation results).

Figure 6 shows frequency estimation histories for these simulations. Again, these results are typical for any number of modes estimated, as long as the Nyquist sampling criterion is met for each mode. Note that all frequencies are correctly estimated within a few periods of vibration.

Figure 7 shows overall shape estimation errors as a function of time. Shape estimation error is defined here as the root-mean-square (RMS) estimation error computed over the entire structure surface. Note that shape is quickly estimated within one or two periods of vibration of the lowest natural

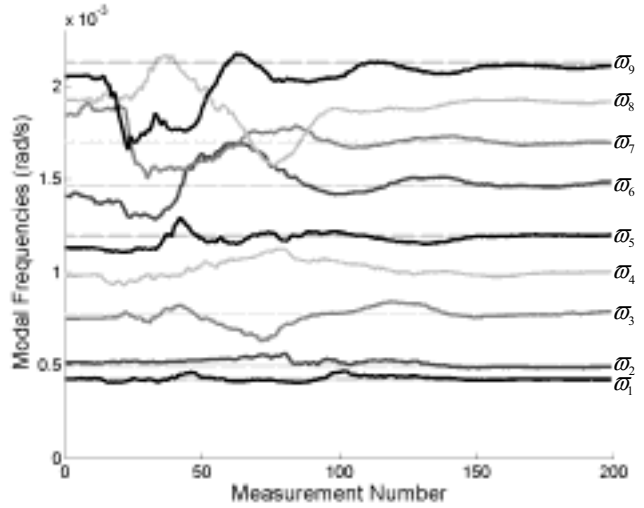

Fig. 6. Frequency estimates (simulation results). Dotted lines indicate true values.

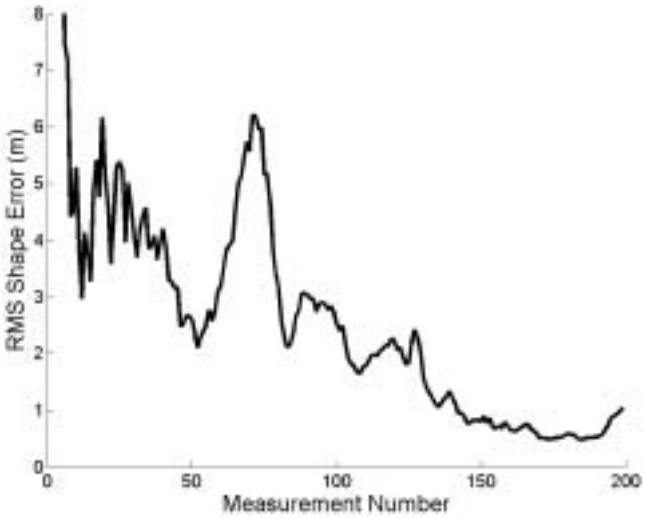

Fig. 7. Shape estimation error vs. time, with all excited modes estimated (simulation results). Amplitude of vibration is approximately 25 m.

frequency. The spike in the estimation error around measurement 70 arises because the process model is nonlinear and many parameter estimates are still converging at that time.

Simulations were used to evaluate the effect of sensor location and field of view on estimator performance. Single and multiple sensors were studied, viewing anywhere from 5% to 100% of the structure, all with similar results to those presented above. The simulations suggest that as long as the modes are observable, estimation is efficient and robust. Increasing sensory noise simply scales up the noise on the coarse estimates $\breve{A}(t)$ (see (4)), which generally only slows the rate of convergence of the Kalman filter.

6.2. Experimental Results

Experiments were conducted at the JAXA Space Center in Tsukuba, Japan using representative structures and sensors to evaluate the performance and practicality of the estimation algorithm. A flexible panel measuring 2.5 m long and 0.5 m wide was mounted on air bearings and placed on a highly polished air table as shown in Figures 8 and 9. One end of the structure was rigidly constrained to ground. Structural vibrations occurred in the horizontal plane orthogonal to the gravitation vector. The periods of vibration for the first five modes were approximately 44, 6.8, 2.6, 1.4, and 0.55 s, respectively. This system emulates a space structure reasonably well since it possesses low damping and sustains vibrations in several modes for many cycles before damping out.

The dynamics of this system can be represented reasonably well using the Bernoulli–Euler cantilever beam model. Here, the analytical solutions for the mode shapes were used in the estimator, although any method of mode shape determination could have been used (finite element analysis, empirical measurement of a scale model, etc.). Initial guesses for the modal frequencies were taken from very rough (one digit precision) measurements using a stopwatch. Certainly, more accurate *a priori* estimates of the mode shapes and parameters could have been used; however, these coarse methods were used to demonstrate the estimator's robustness to *a priori* uncertainty.

For these experiments, a Pulstec Industrial Co., TDS-series 3D laser scanner was used to observe the structure. The scanner was mounted on a robotic manipulator to allow accurate repositioning between experiments (see Figure 9). The scanner has a field of view of approximately 8° by 7° and typically observes only 5 to 30% of the structure's surface area during an experiment. Range measurement noise on the sensor is on the order of 20 mm at a range of 2 m (the approximate distance used in these experiments).

The system captures two range image scans per second, with even scans sweeping upward through space and odd scans sweeping downward. During each asynchronous scan, the system gathers approximately 2000 points, distributed over a 400-ms interval. That is, the last point in each scan is captured approximately 400 ms after the first point. The time delays for all points (i.e., the Δ_k values in (6) for all k) were recorded and provided to the estimation algorithm.

Figure 10 shows typical experimental results for the coarse estimates $\breve{A}(t)$and the Kalman-filtered estimates $\hat{A}(t)$ for several modes of vibration. Note that the Kalman filter performs effectively like a notch filter and removes spurious signals and bias from the coarse estimates.

Figures 11 and 12 show typical experimental results for the estimation of modal frequencies and damping. Frequency estimates converged on the order of two periods of the mode being

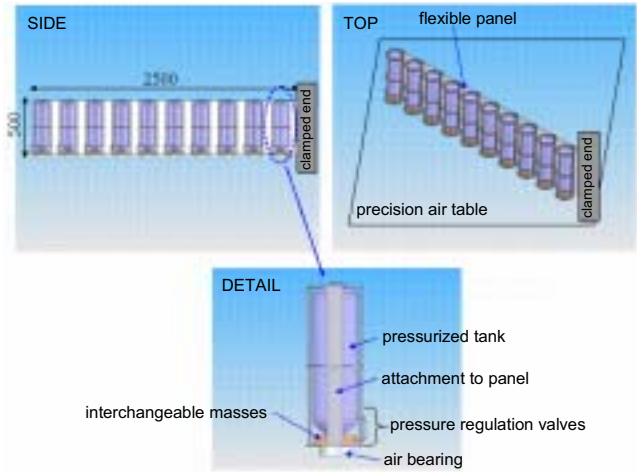

Fig. 8. Schematic of experimental system.

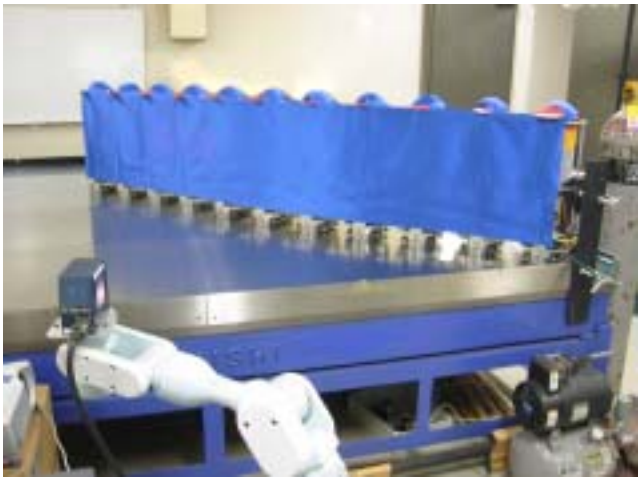

Fig. 9. Photograph of experimental system. Laser rangefinder mounted on manipulator arm can be seen in the foreground at left.

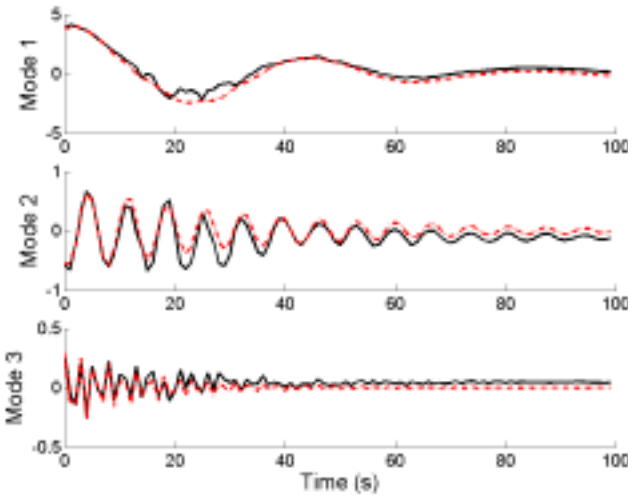

Fig. 10. Coarse estimates of modal coefficients (solid) with Kalman-filtered estimates superimposed (dashed) (experimental results).

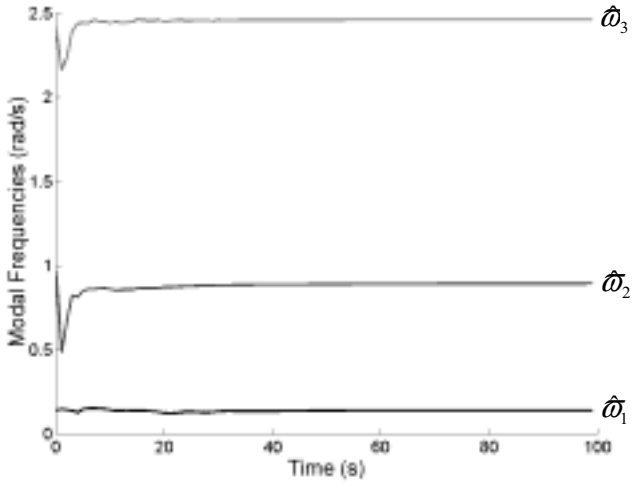

Fig. 11. Modal frequency estimates (experimental results).

estimated. Here, damping has a comparatively small influence on system dynamics and therefore can only be observed over long time intervals, which explains the relatively slow convergence of these parameter estimates. It should be noted that the observability of parameters declines over time in a damped system such as this. Many of the higher modes damped out too quickly to be estimated with reasonable confidence. Table 1 summarizes the mean and standard deviation of the final parameter estimates for the first three modes, recorded over fifteen independent trials. The frequency values are consistent with direct empirical measurements of the structure. It was difficult to obtain a consistent baseline measurement of damping, however, since damping varied somewhat throughout trials due to uncontrolled environmental factors such as micro-scale table contaminants and room temperature to a lesser extent.

The goal of estimation is more than simply observing structural deformations and parameters, however. Knowledge of the dynamic model and the ability to estimate parameters allows the estimator to *predict* future motions and shape of the structure. This predictive capacity is useful and sometimes necessary for certain planning and control tasks such as robotic rendezvous and docking. Figure 13 illustrates the estimated motions of the structure under two different situations. The solid line represents the best estimate the filter can

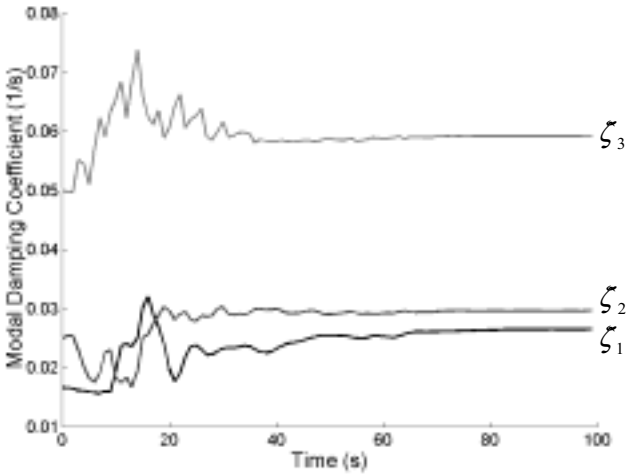

Fig. 12. Modal damping estimates (experimental results).

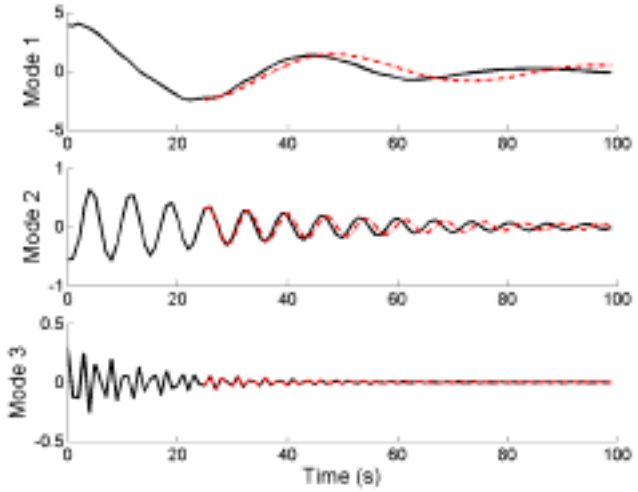

Fig. 13. Coefficient predictions when measurements are halted at time t = 25 (dashed). Solid lines effectively represent the actual coefficients, found by using all measurements through time t = 100.

Table 1. Parameter Estimates After 100 Seconds of Observation, for Fifteen Independent Trials

Mode Number	ω estimate (rad/s)	α estimate (1/s)
1	0.14 ± 0.016	0.033 ± 0.012
2	0.87 ± 0.025	0.070 ± 0.036
3	2.44 ± 0.33	0.146 ± 0.091

achieve, incorporating all measurements from time t = 0 to t = 100. By contrast, the dashed line shows the estimate if the filter receives measurements only during time t = 0 to t = 25 and then predicts the motion for t = 25 to t = 100 by extrapolating from its last estimate. The predictions can be seen to track the actual motions reasonably well for some time after measurements are stopped. Frequency, phase, amplitude, and damping appear to be estimated reasonably accurately by the time the last measurement is processed. Over time, phase error accumulates due to small errors in the frequency estimate, and eventually the prediction loses synchronization with the actual motions.

As one might expect, if the estimator is given more measurements before it begins predicting motion, its parameter estimates will be more accurate and thus motion predictions will track the actual system for a greater length of time. This is illustrated in Figure 14, where the estimator receives twice as many measurements – from time $t = 0 \ldots 50$ – before beginning prediction. The predictions remain synchronized with the actual system for a long period of time because errors in the frequency estimates are very small at the time measurements are halted.

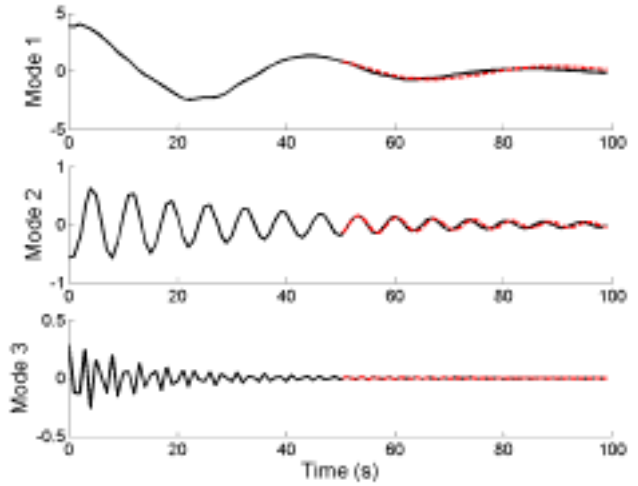

Fig. 14. Coefficient predictions when measurements are halted at time t = 50 (dashed). Solid lines effectively represent the actual coefficients, found by using all measurements through time t = 100.

6.3. Computational Requirements

For such an estimation method to be practical for space applications, it must have a small computational footprint. Typically, space-qualified computation lags the consumer PC industry by an order of magnitude or more in speed.

Table 2 shows the estimator computation time required to process each measurement on a 1 GHz Pentium III processor.

Table 2. Computation Time Per Sample (Seconds)

		Number of Points in Range Image			
		100	1000	10^4	10^5
Number of modes estimated	10	0.030	0.038	0.18	1.4
	20	0.22	0.24	0.65	4.4
	30	0.87	0.89	1.7	9.1
	40	2.1	2.2	3.5	–
	50	4.6	4.8	6.6	–

The table spans the domain of practical interest for large space structures and space qualified vision systems. The empirical relation describing computation time as a function of the number of range points (n) and the number of modes estimated (m) is given approximately by

$$t_{compute} \approx c_1 mn + c_2 m^3$$

where $c_1 \approx 1.4 \times 10^{-6}$ and $c_2 \approx 3.6 \times 10^{-5}$. The cubic term is due to matrix inversions involving matrices of size proportional to m. The bilinear term is due to the inner product computation between range data and each mode shape, which involves summations over a set of size m by n.

Periods of vibration for very large space structures can be on the order of tens of minutes. In practice, sensors may only need to sample at a rate of a few times per minute to reliably observe the motions of the structure. Further, it might only be necessary to observe the first ten or twenty modes in order to obtain good shape estimates. Therefore, even with space-qualified hardware, it seems that the computational requirements of the estimator are manageable for practical implementation.

7. Conclusions

This paper has described a methodology for estimating structural vibrations using range images generated from cooperative teams of sensors. The method uses three distinct parts and exploits a key feature of space applications, which is that the dynamics of objects in space are well-modeled. This feature enables an estimator design that is accurate, efficient, and robust to the challenging sensing conditions found in space.

By design, the method presented here accommodates highly noisy and missing sensor data, the artifacts of harsh sensing conditions such as strong sunlight. The method can handle visual data from both synchronous-capture and asynchronous-capture (raster-scanning) range imaging sensors. The estimator contains a built-in method for computing the observability of modes, which is useful for ensuring the validity of estimates and could be used to optimize sensor placement. The method presented here imposes no restrictions on the motions of the sensors, as long as these motions are known with reasonable accuracy. The sensor localization requirements are not severe and are achievable using various conventional technologies. The computational requirements of the algorithm are also very low, making the method appropriate for real-time implementation on space-qualified hardware.

The method requires only a priori estimates of the mode shapes and initial guesses for the modal frequencies. Analysis has shown that uncertainty in the mode shapes does not degrade estimator performance catastrophically. Simulation and experimental studies have demonstrated the performance and practicality of the method under emulated space conditions.

Acknowledgment

The authors would like to acknowledge Shinji Mitani, Satoshi Suzuki, Kazuyuki Inaba, and Dr. Tatsuya Endo for the design and fabrication of experimental systems and their valuable assistance while conducting experiments; and Dr. Yoshiaki Ohkami, Dr. Mitsushige Oda, Dr. Karl Iagnemma, and the anonymous reviewers for helpful feedback during the development of this work.

This work was supported in part by the Japan Aerospace Exploration Agency (JAXA).

References

Jenkin, M. and Jasiobedzki, P. 1998. Computation of stereo disparity for space materials. *Proc. IEEE International Conference on Intelligent Robots and Systems (IROS).*

Julier, S. J. and Uhlmann, J. K. 1997.A new extension of the Kalman filter to nonlinear systems. Proc. AeroSense: The 11th International Symposium on Aerospace/ Defense Sensing, Simulation and Controls, Orlando, Florida.

Lichter, M. D. 2004. Shape, motion, and inertial parameter estimation of space objects using teams of cooperative vision sensors. PhD thesis, Dept. of Mech. Eng., MIT.

Maghami, P. G. and Joshi, S. M. 1993. Sensor/actuator placement for flexible space structures. *IEEE Trans. on Aerospace and Electronic Systems* 29(2): 345–351.

Mangalgiri, V. 2004. Analysis for the robotic assembly of large flexible space structures. MS Thesis, Dept. of Mech. Eng., MIT.

Mankins, J. C. 1997. A fresh look at space solar power: new architectures, concepts and technologies. Proc. 38th Internationall Astronautical Federation Conference.

Metaxas, D. and Terzopoulis, D. 1993. Shape and nonrigid motion estimation through physics-based synthesis. *IEEE Trans. on Pattern Analysis and Machine Intelligence* 15(6).

Oda, M., Ueno, H., and Mori, M. 2003. Study of the solar power satellite in NASDA. *Proc. 7th International Symposium on Artificial Intelligence, Robotics, and Automation in Space: i-SAIRAS 2003*, NARA, Japan, May.

Scattolini, R. and Cattane, N. 1999, Detection of sensor faults in a large flexible structure. *IEE Proceedings: Control Theory and Applications* 146(6) : 383–388.

Staritz, P. J., Skaff, S., Urmson, C., and Whittaker, W. 2001. Skyworker: a robot for assembly, inspection and maintenance of large scale orbital facilities. *Proc. 2001 IEEE International Conference on Robotics and Automation (ICRA 2001)*, Seoul, Korea, May, pp. 4180–4185.

Stieber, M. E., Petriu, E. M., and Vukovich, G. 1996. Systematic design of instrumentation architecture for control of mechanical systems. *IEEE Trans. on Instrument and Measurement* 45(2): 406-412.

Tse, D.N.C. and Heppler, G. R. 1992. Shape determination for large flexible satellites via stereo vision. *AIAA Journal of Spacecraft and Rockets* 29(1): 108–117.

Ueno, H., Nishimaki, T., Oda, M., and Inaba, N. 2003. Autonomous cooperative robots for space structure assembly and maintenance. *Proc. 7th International Symposium on Artificial Intelligence, Robotics, and Automation in Space: i-SAIRAS 2003*, NARA, Japan, May.

Vergauwen, M., Pollefeys, M., and Van Gool, L. J. 2003. A stereo-vision system for support of planetary surface exploration. *Machine Vision and Applications*, 14(1): 5–14.

Wakabayashi, Y., Ohkami, Y., Miyata, M., et al. 1999. A compact laser range finder for space applications. *Proc. SPIE*, Vol. 3714: *Enabling Photonic Technologies for Aerospace Applications*, edited by A. R. Pirich and E. W. Taylor, pp. 131–138.

Zhang, H.-H. and Wu, H.-X. 1993. Identifiability of flexible space structures. *Proc. IEEE Conference on Decision and Control*, Vol. 2, December, pp. 1488–1493.